CHAPTER 5

MAGNETO-FLUORESCENT HYBRID NANOSYSTEM: DEVELOPMENT AND CHARACTERIZATION

MAGNETO-FLUORESCENT HYBRID NANOSYSTEM: DEVELOPMENT AND CHARACTERIZATION

5.1 Introduction

In the recent years, nanoparticles have played a pivotal role in the advancement of the modern biomedicine field. Indeed, some instances are there, where the nanoparticles are only applicable for analysis and therapies [1-5]. Inorganic magnetic nanoparticles (MNPs) have specifically attracted attention in this field due to their unique ability of responding to an external magnetic field, which can lead to successful applications, like protein separation, drug delivery and MR contrast imaging. At the same time, quantum dots (QDs), as fluorescent probes have emerged with immense potentials for cell labeling, tracking of cell migration and *in vivo* imaging [6-9]. In the next generation, peoples have conceptualized integrating these functionalities into a single system, named HYBRID NANOSYSTEM. The unique advantage of this nanoprobe is that different diagnostic functionalities or diagnostic-therapeutic can be performed simultaneously through a single entity [10-14].

The integration of fluorescence imaging (FI) with MR imaging (MRI) will be a significant step towards the development of innovative noninvasive imaging techniques. With this concept in mind, the idea of developing magneto-fluorescent hybrid nanomaterial has been conceived here, which can be used as a dual imaging (magnetic and fluorescent) probe. An attempt has been made in this thesis to bring this novel concept into reality. In the present chapter, the primary objective was laid down to develop an array of magneto-fluorescent multimodal hybrid nanosystems. In achieving the aforementioned goal, the pristine magnetic nanosystems and quantum dots were synthesized and optimized based on their physical properties.

Here, a facile one-pot polyol synthesis technique of core/shell magneto-fluorescent hybrid nanosystems capped with GSH molecules is described. The used one-pot synthesis is advantageous, as the synthesized nanoparticles are obtained directly in the aqueous phase without any post-synthesis ligand exchange. The L-glutathione (-glu-cys-gly, GSH) is a tripeptide, natural reducing molecule, which is most abundant non-

protein thiol in mammalian cells [15]. This molecule is involved in major physiological functions such as detoxification, redox-buffering, and antioxidant activity. The FePt NPs capped with thioglycolic acid (in **Section C** of **Chapter 3**) was used as core and the fluorescent QDs were attached to it as a shell (**Chapter 4**). **Section A** of **chapter 5** describes the one pot facile synthesis of hydrophilic FePt@CdX (X= Te or Se) core/shell multimodal hybrid nanosystem. **Section B** of **chapter 5** describes the one pot facile synthesis of hydrophilic FePt@CdS core/shell multimodal hybrid nanosystem, where glutathione is used as a sulfur source as well as the capping agent. The physicochemical properties of FePt@CdTe, FePt@CdSe, and FePt@CdS core/shell multimodal hybrid nanosystems were studied in contrast to the pristine magnetic nanosystem and quantum dots.

5.2 Materials and methods

This section enlists the materials used and the procedures adopted for the synthesis of magneto-fluorescent hybrid FePt@CdTe, FePt@CdSe, and FePt@CdS nanosystems. For the synthesis and purification procedure of the hybrid nanosystems, analytical grade materials were used as received without purification. For the development of magnetic core, the metallic precursors, Pt (II) acetylacetonate [$Pt(acac)_2$, 99.99%] and Fe (III) acetylacetonate [$Fe(acac)_3$, 99.95%], were procured from Sigma-Aldrich. Sodium borohydride ($NaBH_4$) and thioglycolic acid (TGA, 80%), used as reducing and capping agents respectively, were procured from Merck Millipore. Ethylene glycol ($C_2H_6O_2$), ethyl alcohol, and acetone were procured from Merck Millipore. Cadmium chloride monohydrate ($CdCl_2.H_2O$ 99%) was used as a Cd source whereas the sodium tellurite (Na_2TeO_3, 100 mesh, 99%) from Sigma-Aldrich was used as a tellurium source. Selenium powder (Se, 100 mesh, 99.99%) from Sigma-Aldrich was used as a selenium source in GSH capped FePt@CdSe hybrid nanosystem. Glutathione (GSH, $C_{10}H_{17}N_3O_6S$, 99%) from Sisco Research Laboratory (SRL) was used as a capping agent for the aforementioned hybrid nanosystems as well as sulfur source for the formation of GSH capped FePt@CdS hybrid nanosystem. Type 1 water of Milli-Q purification system was used for purification, characterization, and experimental processes.

Section A

5.3 Synthesis of magneto-fluorescent hybrid FePt@CdTe and FePt@CdSe nanosystems

A facile one-pot method was adopted for the synthesis of hydrophilic FePt@CdX (X= Te or Se) core/shell multimodal hybrid nanosystem.
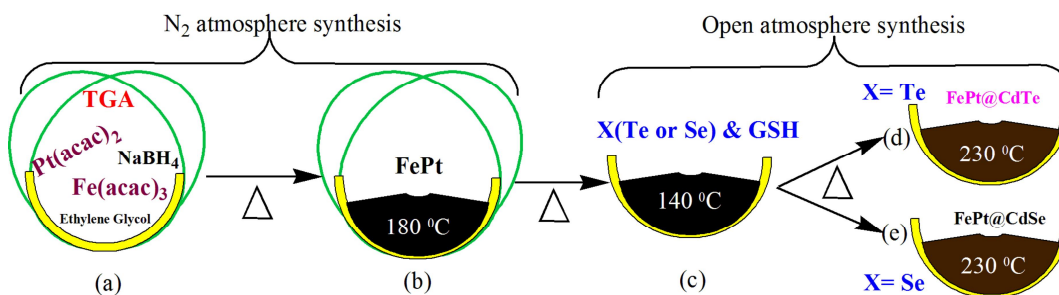

Figure 5.1 Schematic diagrams represent the synthesis of magneto-fluorescent hybrids FePt@CdTe and FePt@CdSe nanosystems

FePt MNPs were developed by a facile polyol process (as described in **Section C** of **Chapter 3**) where 25 ml of ethylene glycol, 1 mmol Pt(acac)$_2$ and 4 mmol NaBH$_4$ were added initially in a three-necked flask under N$_2$ atmosphere at room temperature [16]. After attaining the temperature of 100 $^\circ$C, 2 mmol of Fe(acac)$_3$ was added along with 200 µl of TGA. The solution was kept under N$_2$ atmosphere and heated up to 180 $^\circ$C at the rate of 1 $^\circ$C per min (**refer figure 5.1 (a) & (b)**). After that, the solution was cooled down to 100 ℃ temperature under inert atmosphere. As-prepared TGA capped FePt magnetic nanoparticles acted as the core for the preparation of magneto-fluorescent hybrid nanosystems. The sources used for Cd, Te and Se were CdCl$_2$.H$_2$O, Na$_2$TeO$_3$ and Se powder in hybrid nanosystem synthesis. The molar ratio of Cd with Te/Se precursor was kept to 5:1 in the reaction mixture. The following reaction was carried out in ambient atmosphere. The Cd precursor (2.5 mmol in 5 ml ethylene glycol) was added to the reaction vessel at the reaction temperature 100 ℃. The temperature was further increased to 140 ℃ and then the X (Te/Se source) was added (0.5 mmol in 5 ml ethylene glycol) in the reaction vessel. After 15 minutes, 0.25 mmol glutathione was added in the reaction vessel at temperature 140 ℃ (**refer figure 5.1 (c)**). Then, the temperature was increased at the rate of 1 ℃/min up to 230 ℃ (**refer figure 5.1 (d) &**

(e)). After this, the reaction was stopped and the reaction vessel was allowed to cool down naturally to room temperature. The precipitate was separated from the reaction mixture by centrifugation and washed three times using hexane, isopropyl alcohol, and methanol to remove the residual surfactants. The purified mass obtained was used for further characterization. It is notable here that the synthesis of the shell was carried out in the open atmosphere here. The proper formation of the shell was not observed when this synthesis was carried out in N_2 atmosphere.

5.4 Characterization

The synthesized QDs were characterized using several techniques for in-depth understanding of properties.

5.4.1 Results and discussion

X-ray diffraction (XRD) studies were carried out for the structural characterization of quantum dots and hybrid nanosystem.

In the **figure 5.2**, the XRD pattern of FePt nanoparticles is shown, which exhibits the presence of (111), (200), (220) and (311) planes at 2 values of 40.5°, 46.4°, 67.8° and 82.1° respectively. Obtained peak positions were indexed according to the standard JCPDS files (JCPDS 29-0717), which indicate the presence of fcc FePt phase. In the case of CdTe QDs, three distinct peaks at 2 values of 23.7°, 39.2° and 46.4° are observed corresponding to (111), (220) and (311) planes respectively. Here, all the diffraction peaks are corroborating to fcc CdTe structure (JCPDS 89-3053). The diffraction pattern of CdSe QDs indicates the presence of (100), (002), (101), (110), (103) and (201) planes at 2 values of 23.8°, 25.3°, 27.0°, 41.9°, 45.8° and 50.6° respectively, indicating hexagonal wurtzite CdSe crystal structure (JCPDS 77-2307).

The presence of the peak at 2 = 40.5° for both hybrid nanosystems (indicated by black arrow), confirm the presence of (111) plane of FePt NPs. This peak is also emerged at the same position in the pristine FePt nanoparticles. In FePt@CdTe, there is another peak at 2 ~ 25°, is due to the formation of CdTe nanocrystal. Except (111) plane of FePt NPs, FePt@CdSe system also has some additional peaks at ~ 26°, 44°, 47° and

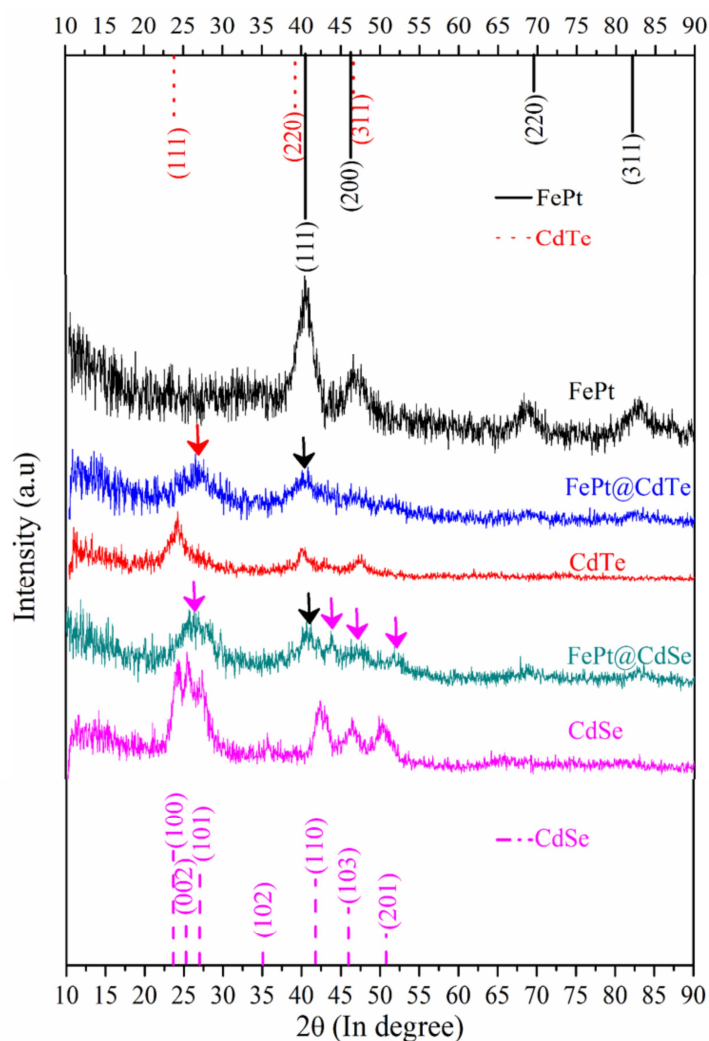52°, corresponding to (100), (110), (103), and (201) planes of CdSe crystal lattice (indicated by pink arrow).

Figure 5.2 XRD patterns of pristine and magneto-fluorescent hybrid nanosystems

In the case of both hybrid systems, 2θ peak positions for CdTe and CdSe are observed to be shifted to higher values as compared to pristine systems, which indicate the crystal lattice disorder induced strain occurring at the time of hybrid formation. The possibility of CdS crystal formation at the surface in both hybrid systems as well in pristine quantum dots systems can∅t be ruled out [17, 18].

The HRTEM micrographs of FePt@CdTe and FePt@CdSe are shown in **figure 5.3 (a)** and **(b)** respectively, while **figure 5.3 (c)** and **(d)** shows the SAED patterns of

FePt@CdTe and FePt@CdSe hybrid nanosystems. The EDX spectrum of FePt@CdTe and FePt@CdSe are shown in **figure 5.3 (e)** and **(f)** respectively.
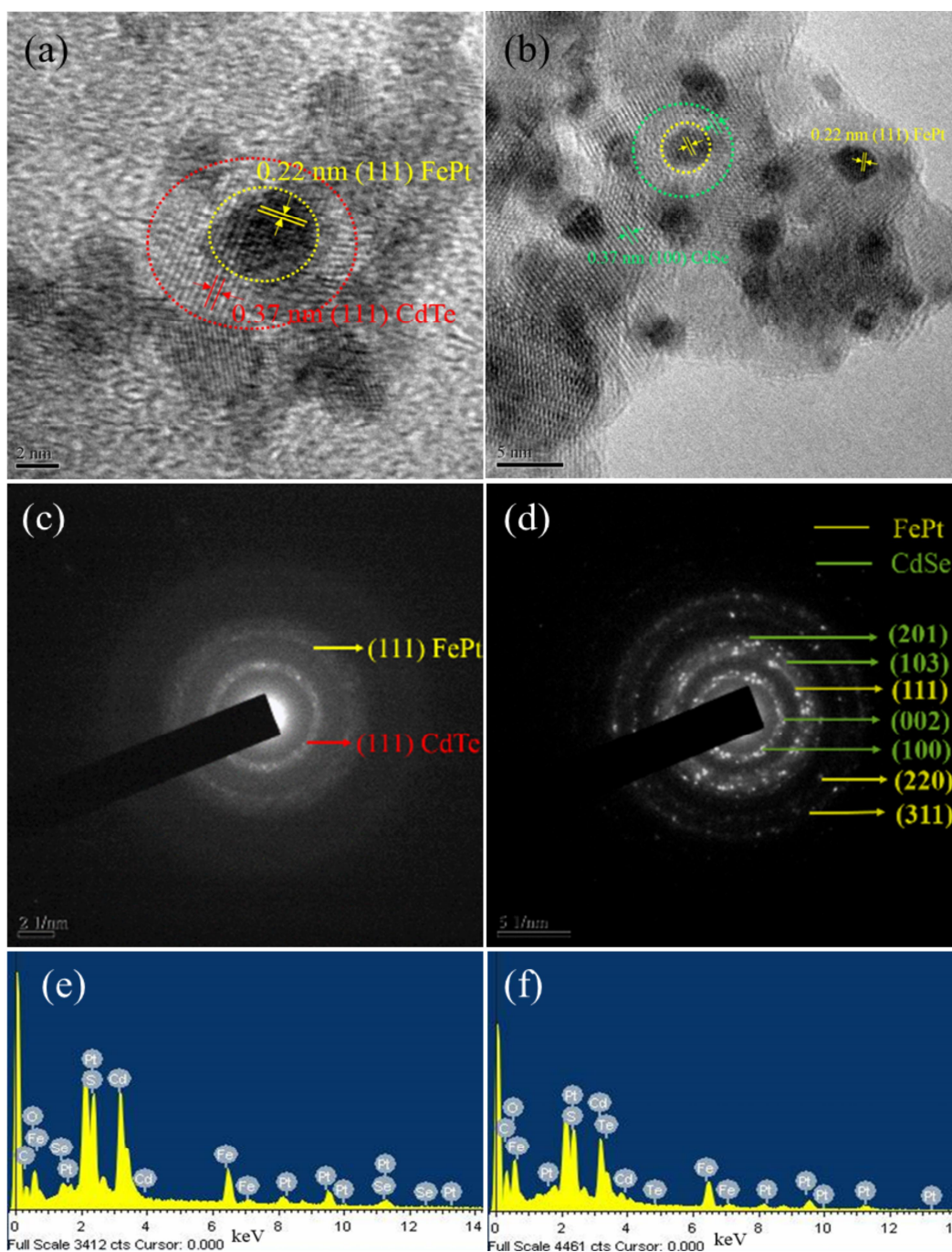

Figure 5.3 (a) HRTEM, (c) SAED image and (e) EDX spectrum of FePt@CdTe whereas the (b), (d) and (f) represent the HR-TEM, SAED and EDX spectrum of FePt@CdSe systems respectively

The HRTEM micrographs (**figure 5.3 (a)**) of FePt@CdTe show the distinct lattice fringes of FePt (core) and CdTe (shell), corresponding to the interplanar d-spacing of 0.22 nm and 0.37 nm respectively. The SAED pattern analysis of FePt@CdTe (**figure 5.3 (c)**) reveals the fcc phase of FePt and fcc phase of CdTe crystal.

HRTEM micrograph of FePt@CdSe shown in **figure 5.3 (b),** shows the core-shell structure of the hybrid nanosystem. The HRTEM image of FePt@CdSe sample indicates the interplanar spacing of 0.22 nm corresponding to (111) plane of FePt while the shell shows an interplanar spacing of 0.37 nm corresponding to (100) plane of CdSe nanocrystal. The SAED pattern analysis (**figure 5.3 (d)**) reveals the presence of (111), (220) and (311) planes corresponding to fcc phase of FePt while (100), (002), (103) and (201) planes correspond to the hexagonal wurtzite phase of CdSe crystal. It is evident that the d-spacing calculated from the SAED pattern analysis are in good agreement with the analysis of XRD pattern. In HR-TEM micrograph of FePt@CdTe and FePt@CdSe, we find that there is a change in contrast (center is darker than peripheral) in a single nanosystem. It provides the indirect approval of core-shell structure formation in hybrid nanosystems.

The EDX spectrum of FePt@CdTe shown in **figure 5.3 (e)** confirms the presence of peaks of the element present in the sample - C (K line, 0.2 keV), O (K line, 0.5 keV), S (K line, 2.3 keV), Fe (L line, 0.7 keV; K line, 6.4 keV; K line, 7.1 keV), Pt (M line, 2.0 keV; L line, 9.4 keV), Cd (L line, 3.1 keV), and Te (L line, 3.7 keV). In the EDX spectrum of FePt@CdSe (**figure 5.3 f),** Te peak was replaced by Se peak (K line, 11.2 keV; L line, 1.3 keV), while all other elemental peak positions were observed to be same. **Table 5.1 (a)** and **(b)** indicates the average quantitative data of FePt@CdTe and FePt@CdSe hybrid nanosystems taken from five spots. In both the samples, the atomic ratio of Fe and Pt is 1:1 whereas, the Cd:X (X= Te/Se) ratio is around 5:1.

The interactions between GSH and hybrid nanosystems were studied by FTIR spectroscopy, zeta potential, and thermogravimetric analysis. The reaction was carried in alkaline (pH 10) condition. The comparative FTIR spectra of pure GSH powder and TGA capped FePt and GSH capped FePT@CdTe and FePt@CdSe hybrids are presented in **figure 5.4 (a).** The L-glutathione (GSH) is a tripeptide molecule made up

from a molecule of L-glutamic acid, L-cysteine, and glycine amino acid (-glu-cys-gly). GSH molecule is rich in functional groups containing two peptide or amide (-CONH-) bond, two -COOH and one -NH_2 group.

Table 5.1 Quantitative data from EDX analysis of GSH capped (a) FePt@CdTe (b) FePt@CdSe

(a)

Element	Weight%	Atomic%
C K	16.52	35.13
O K	31.17	49.77
S K	6.50	5.18
Fe K	6.05	2.77
Cd L	17.56	3.99
Te L	3.79	0.76
Pt M	18.42	2.41

(b)

Element	Weight%	Atomic%
C K	9.10	26.33
O K	20.81	45.20
S K	9.53	10.33
Fe K	6.48	4.03
Se L	3.67	1.61
Cd L	26.71	8.26
Pt M	23.71	4.22

The FTIR spectrum of pure GSH molecule (**figure 5.4 (a)**) shows two strong bands at 3345 and 3250 cm^{-1}, which are assigned to the N-H stretching vibration from the NH_2 molecules present in the glutamic acid residue, merged into a broadband in the range of 3200-3500 cm^{-1} for both hybrid nanosystems. The bands present at 3127 and 3021 cm^{-1} in pure GSH molecule is ascribed to N-H stretching vibration of NH_3^+ [19].
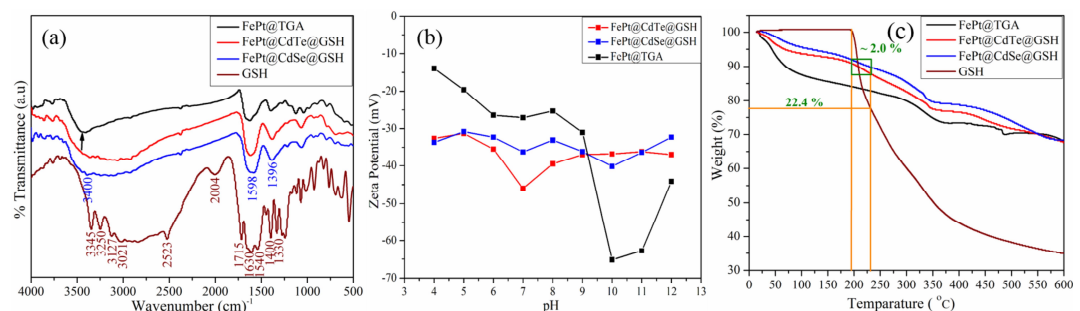

Figure 5.4 (a) Comparative FTIR spectra of TGA capped FePt, pure GSH and GSH capped FePt@CdTe, FePt@CdSe hybrid nanosystems, (b) zeta potential of hybrids and TGA capped FePt MNPs (c) A comparative TG analysis of pure GSH, hybrids and TGA capped FePt MNPs

A strong band at 2523 cm^{-1}, attributed to the -SH stretching vibrations, is absent in both the hybrid systems indicating deprotonation of a thiol group and coordination of the thiol group to particles. The combined bands of asymmetric NH$_3^+$ bending vibration and hindered NH$_3^+$ rotation at 2004 cm^{-1} in free GSH, disappeared in GSH capped hybrid nanosystems, indicating that the amino group coordinated to surface of hybrid nanosystems under alkali condition due to the deprotonation of amino group at pH 10. The carboxylic C=O stretching vibration of the -COOH group from glycine residue is expressed by 1715 cm^{-1} peak in pure GSH molecule and shifted to lower frequencies in the hybrid nanosystems, possibly due to the deprotonation of -COOH group due to alkaline condition. The characteristic C=O stretching (amide I) and N-H bending vibration (amide II) of amide bond expressed at 1630 and 1540 cm^{-1} in pure GSH molecule are merged into a single band centering at 1580 cm^{-1} in hybrid nanosystems. The CH$_2$ bending vibration arises in the range of 1400 cm^{-1} and the band at 1330 cm^{-1} is attributed to the C-N stretching vibration in pure GSH molecule. The disappearance of the -SH stretching vibrational peak, the almost disappearance of the N-H and the weakening of the amide bond clearly indicates that GSH may combine onto the surface of the QD shell through the -SH and -NHR groups [20, 21].

Figure 5.4 (b) indicates zeta potential ( ) value of GSH capped hybrid nanosystem and thioglycolic acid capped FePt nanoparticles, the core in hybrid nanosystems. The   is an indicator of particles surface charge and stability of the system in a solution. At lower pH value (pH<3), the GSH molecules are behaving positively charged whereas at the pH 4 to 12, it is showing negatively charged. In the pH range from 4 to 12, the surface charge   shows a negative potential value around 35 mV suggesting increased repulsion and stability of hybrid nanosystems in aqueous solution [22, 23]. The observed variation from the potential of TGA capped FePt core system indicates the formation of a shell (CdTe/Se) and encapsulation with the ligand (GSH) during the synthesis process.

Figure 5.4 (c) indicates thermogravimetric analysis study of FePt@CdTe and FePt@CdSe hybrid nanosystems coated with glutathione, FePt coated with thioglycolic acid and pure GSH molecules. The two mass loss peaks at ~ 197 °C and 350 °C of pure GSH and hybrid nanosystems are arising from the pyrolysis of the oxygenated functional groups and NHS moieties of GSH molecule respectively. It is seen that the

pure GSH molecules are stable till 197 °C. The hybrid nanosystem starts to lose mass upon heating beyond 197 °C, which can be attributed to the loss of absorbed water molecules [24]. Here, the maximum reaction temperature was around 230 °C for the synthesis of hybrid nanosystem. At this temperature, it is evident that the pure GSH molecules lose almost 22% of their weight. Therefore, the hybrid nanosystem loses almost 2.2 % weight within the temperature range of 197 °C to 230 °C, confirming the stability of GSH on hybrid nanosystems and absence of free GSH molecules after purification. Based on the XRD, HR-TEM, FTIR, zeta potential and TGA studies, a schematic model for the FePt@CdX (X= Te/Se) is proposed in the **figure 5.5** which shows the arrangement of the core-shell hybrid nanosystem. The core has magnetic FePt nanoparticles whereas the shell is made up of CdX (X= Te/Se) and the uppermost layer is probably made up of CdS. The S atom of GSH is responsible for the formation of CdS layer.
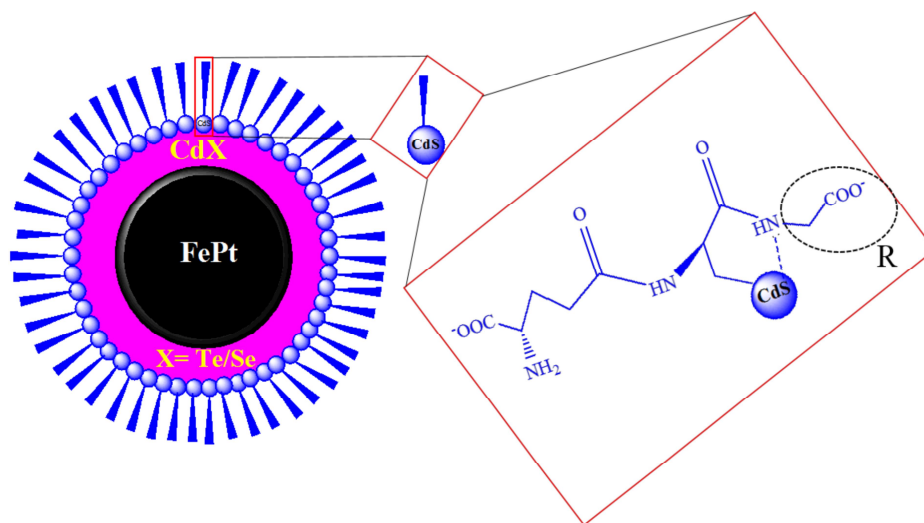

Figure 5.5 Arrangement of core/shell FePt@CdX, where X= Te/Se

Quantum dots absorb photons of light and then re-emit longer-wavelength photons instantaneously. The representative UV-vis absorption and PL spectra of FePt@CdTe and FePt@CdSe QDs in water are shown in **figure 5.6 (a).** Both hybrid systems do not exhibit a well-defined absorption feature (peak). It may be due to less concentration of hybrid systems in aqueous solution. The pristine and hybrid nanosystems were excited at the different wavelength between 300-550 nm whereas the maximum PL intensity observed at wavelength 325 nm (**refer to figure 5.6 (b)**). For pristine QDs, the

emission peak is observed around 400 nm, while, for the hybrid nanosystems, the emission peaks are observed little bit red-shifted [25]. In addition, two newly evolving peaks around 530 nm are observed for both hybrid systems. These two new peaks may be due to the newly developed defect states of quantum dots during hybrid formation. The decrease in the intensity for the hybrid nanosystems as compared to the pristine QDs may be associated with FePt induced quenching of their emission property [26].
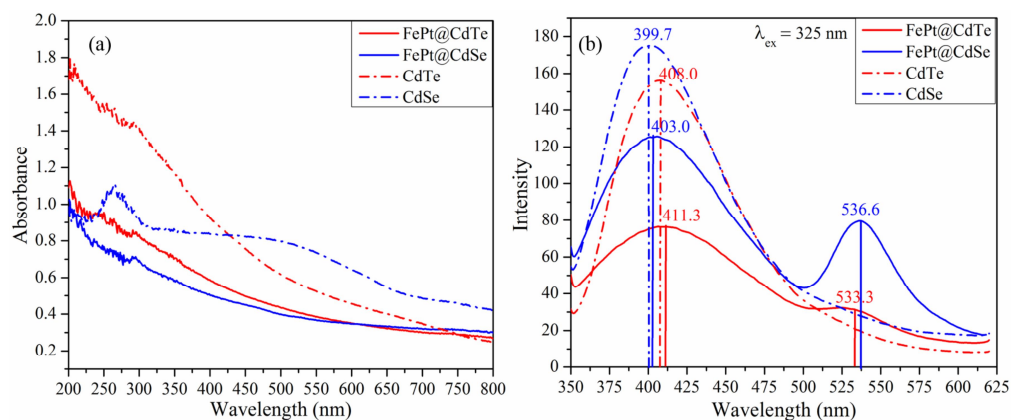

Figure 5.6 (a) UV-vis absorbance and (b) PL of pristine CdTe and CdSe and hybrid FePt@CdTe & FePt@CdSe nanosystem in aqueous suspension. PL excitation wavelength was 325 nm

Like the pristine systems, PL spectra of hybrid systems also consist of three peaks (shown in figure **5.7 (a)** and **(b)**). It is observed that from pristine to hybrid systems, all peaks were broadened and red-shifted. The observed broadening and red-shifting might be due to the new morphology of the quantum dots in hybrid systems. It is worth mentionable that the emissions peaks observed in hybrid nanosystems are not newly originated, only shifted and broadened from pristine to hybrid structure due to the structural evolution of semiconductor material. The origin of emission peaks and their evolution during pristine to hybrid systems were realized by analyzing TRPL (time resolved photoluminescence) data.

TRPL of hybrid nanosystems are shown in **figure 5.7 (c)** and **(d)** along with their respective PL spectra, were best fitted with the tri-exponential decay function as given below-

$$I = A_1 \exp\left(-\frac{t}{1}\right) + A_2 \exp\left(-\frac{t}{2}\right) + A_3 \exp\left(-\frac{t}{3}\right)$$

Where, I is the PL intensity, A_1, A_2 and A_3 represent the amplitudes of three decay processes, t-decay time, $_1$, $_2$ and $_3$ represent the three decay lifetimes. Values of lifetime components and their amplitudes (%) for each hybrid system along with the respective pristine system are shown in **table 5.2**. The average lifetime for each TRPL data is calculated using the following equation:-

$$\langle \tau \rangle = \frac{\sum_i A_i \tau_i^2}{\sum_i A_i \tau_i}$$

*YS (%) - percentage amplitude of the fast component
*YL (%) - percentage amplitude of the longer component.

These are calculated using the equation $\quad Y_i = \frac{A_i}{\sum_i A_i} \times 100$

The fast lifetime component might be due to the direct band-edge excitonic recombination, while other two longer components can be observed due to the radiative recombination of electrons and holes at localized surface states [27, 28]. It is interesting to see in the case of pristine systems, that the amplitudes of the fast components are significantly high than that of the longer components. This implies that the band-edge type emission for the pristine system is dominated over the surface related emission. However, for the hybrid systems, the amplitudes of the fast components are somehow suppressed with the increase in the longer components. This is not surprising, as it is usual to have more surface states due to defects at the interfaces of semiconductor and magnetic components in the hybrid systems.

But, the interesting aspect is that the average lifetimes of charge carriers are found to be increased from pristine to hybrid systems. The increase in the average lifetime signifies the radiative emission stability of the systems. Thus, it can be told that the luminescence property has been improved significantly from pristine to hybrid systems and it is fascinated by the relative increment in the stable surface mediated emission. The improved luminescent property is supported by the calculated quantum yield (QY) values shown in **table 5.3,** whereas**,** fluorescence micrographs of pristine QDs and hybrid nanosystems shown the in the **figure 4.9 & 4.10 (section A; chapter 4)** and **figure 6.4 & 6.5** in next chapter in next chapter respectively.
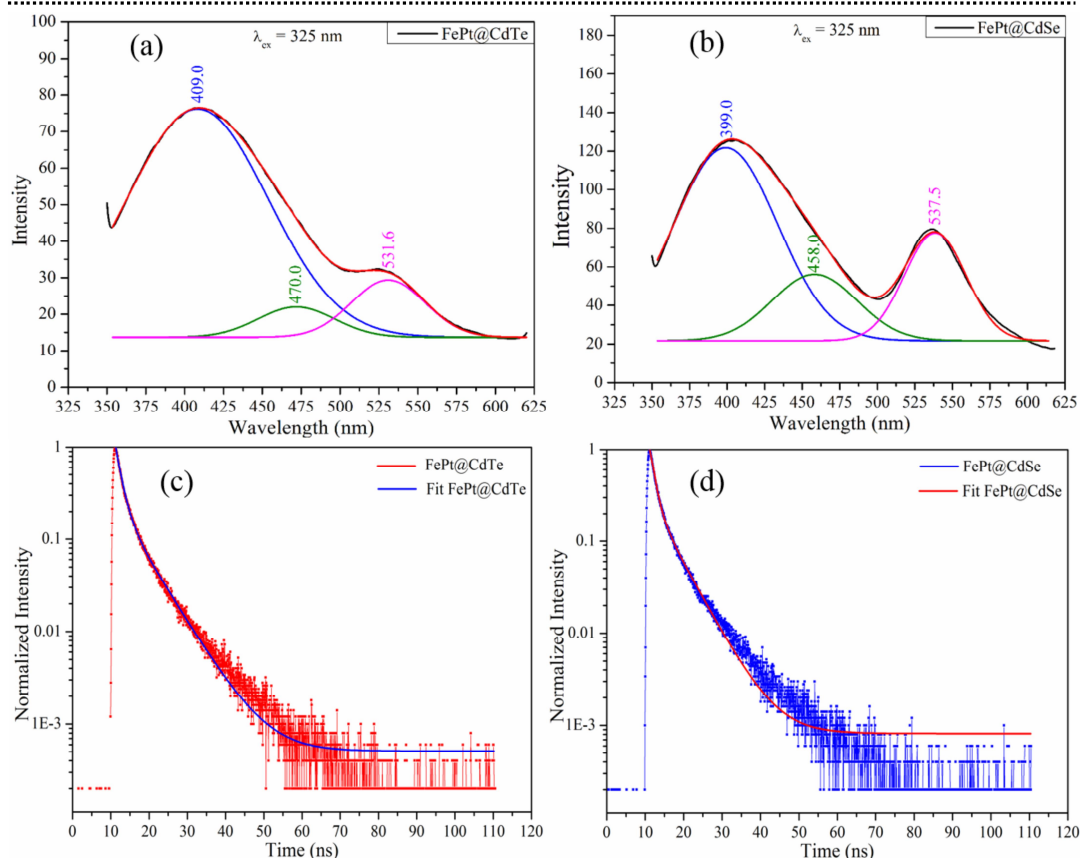
Figure 5.7 Deconvoluted PL spectra (a & b) and TRPL characterization of (c & d) of FePt@CdTe and FePt@CdSe hybrid nanosystems respectively

For both the hybrid systems, it is observed that the values of shorter decay components got dramatically lengthened than those of the respective pure systems. Since, the hybrid systems carry more surface defects, so photo-excited excitons have more tendency to relax favorably through the dense surface states. As a result, this bypass process minimizes the population of photo-excited electrons and holes at the core states and hence increases the lifetime. For the hybrid systems, it is also observed that all the peaks are broadened significantly and defect related peaks are shifted abruptly to the longer wavelengths. The broadening can be related to the enhanced polydispersity of the semiconductor nanocrystals during hybrid formations. Again XRD results show the existence of CdS in the hybrid systems. The CdS can be in two forms, (i) separated CdS nanocrystals or (ii) as the shell material over CdTe and CdSe quantum dots. In the first case, PL spectra should be broadened as CdS gives broader defect dominated emission peaks and in the second case PL spectra are believed to be red-shifted due to the leakage

exciton to the CdS shell. So, seeing the nature of the PL spectra of the hybrid systems, it can be argued that in the hybrid systems, CdS nanocrystals are present in the form of shell material, resulting broadening as well as red-shifting of the PL emission peaks [29].

Table 5.2 Decay components obtained from TRPL results for both pristine and hybrid nanosystems

Systems	Decay components						
	τ_1 (ns)	YS (%)*	τ_2 (ns)	YL$_1$ (%)*	τ_3 (ns)	YL$_2$ (%)*	$\langle \tau \rangle$ (ns)
CdTe	0.088	95	1.71	4.23	7.20	1.35	3.29
FePt@CdTe	0.289	67	1.9	25.37	6.84	6.8	3.64
CdSe	0.0496	97.9	1.72	1.64	7.67	0.47	2.9
FePt@CdSe	0.32	67.9	1.9	25.85	7.12	6.24	3.62

Table 5.3 Comparative Quantum yield (QY) values of pristine and hybrid nanosystems

S. No	Systems	Quantum Yield (%)
1	CdTe	0.98
2	FePt@CdTe	1.14
3	CdSe	1.71
4	FePt@CdSe	2.31

Figure 5.8 shows the M-H plots up to 9 T for the pristine as well as for both the hybrid systems at different temperatures. It is seen that saturation magnetization values of pure FePt nanosystem is decreased significantly after hybrid formations, which is obvious due to the presence of nonmagnetic semiconductor shell. For FePt@CdTe system coercivity and remanence values are observed to be smaller than those of FePt@CdSe system. This can be related to either stronger dipolar interaction among FePt nanoparticles in the FePt@CdTe hybrid system or heavier shell growth of FePt@CdSe [30, 33].
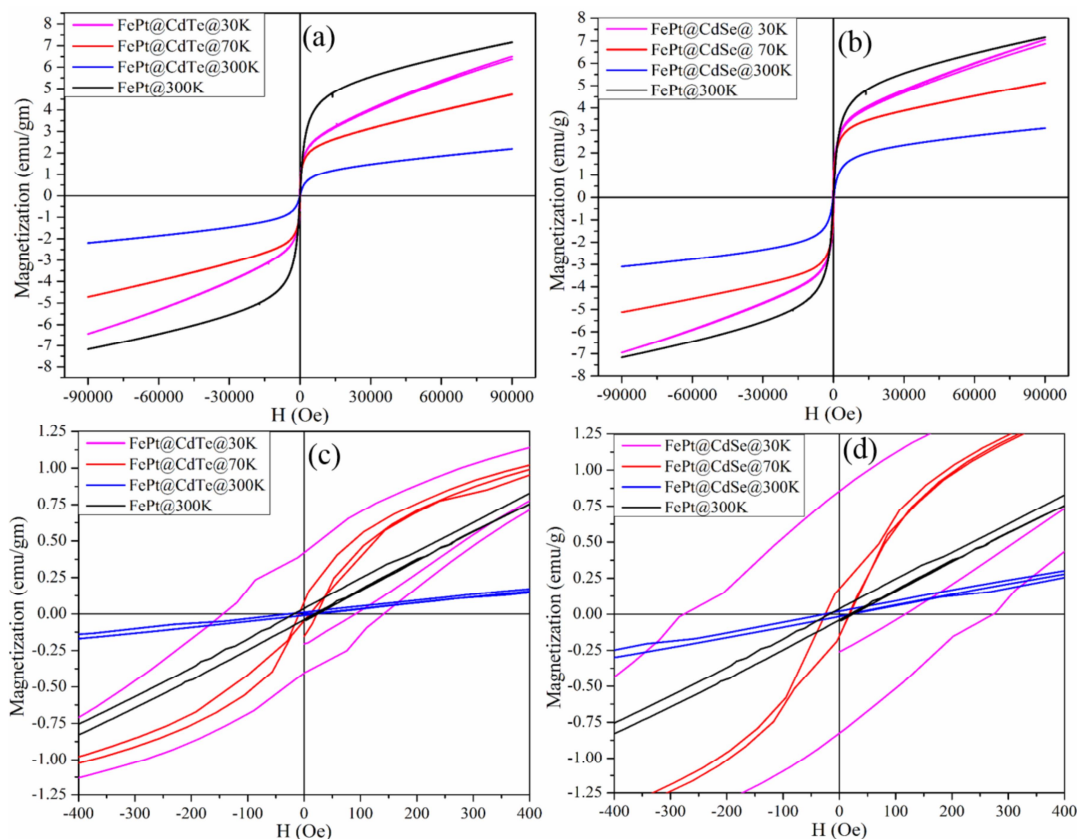
Figure 5.8 M-H measurements of pure and hybrid nanosystems at different temperatures (a & b), with their enlarged plots (c & d)

The observed low values of coercivity at 300 K and blocking temperature well below 300K (shown in Fig. 5.9) confirm the superparamagnetic characteristic of pristine and hybrid nanosystems. **Figure 5.9** shows the zero-field-cooled (ZFC) and field-cooled (FC) magnetization curves of the pristine and the hybrid nanosystems. In ZFC measurements, the samples are initially cooled down in the absence of magnetic field from 300K to 5K and then the magnetization was measured from 5K to 300K in the presence of a small field 100 Oe. On the other hand for FC measurements, the sample was cooled from 300K to 5K in the presence of an applied field of 100 Oe and subsequently magnetization was measured with the same field during warming. The temperature at which ZFC shows a maximum is called the superparamagnetic blocking temperature (T_B) and this is found to be 75 K, 72 K and 63 K for FePt, FePt@CdSe, and FePt@CdTe nanosystems respectively. Above T_B, thermal vibrations are strong enough to randomize the magnetic moments leading to superparamagnetic behavior. The lower

value of blocking temperature implies the low magnetocrystalline anisotropy energy, which is generally obtained for superparamagnetic nanoparticles.
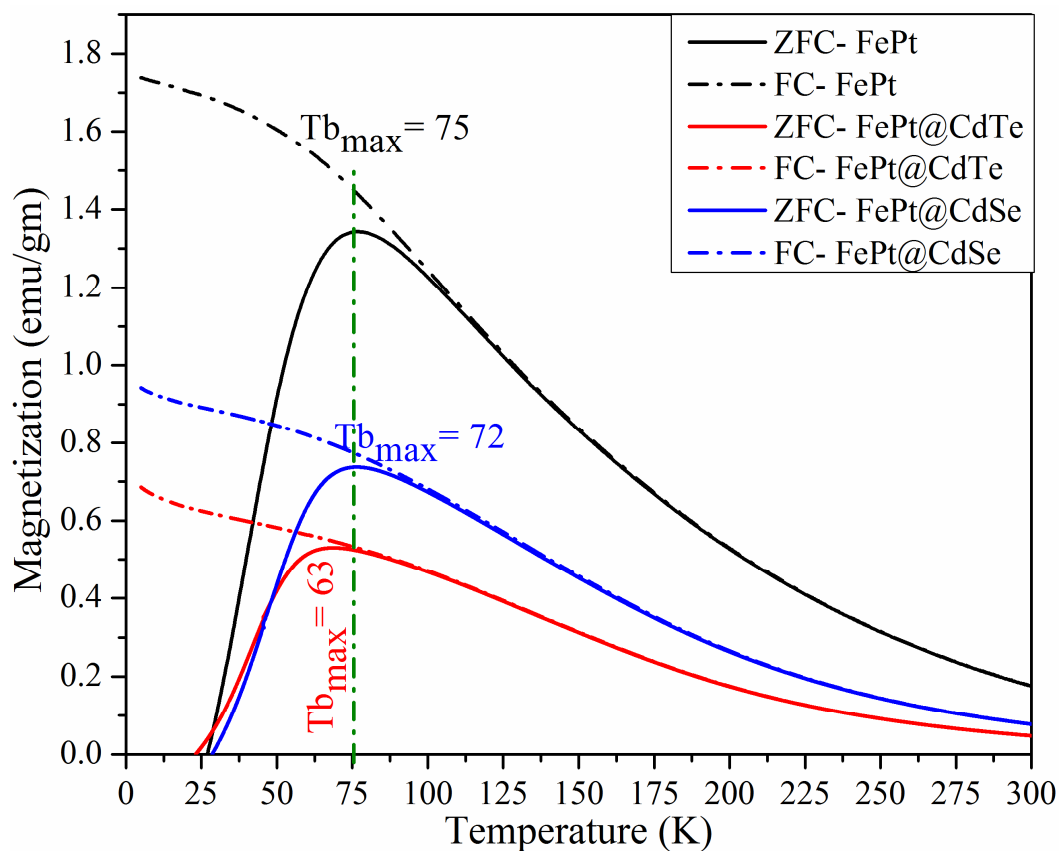

Figure 5.9 Temperature dependent magnetization measurements (M-T with ZFC/FC conditions) of both pristine and hybrid nanosystems

Here, the observed lowering of blocking temperature for the hybrid systems against the pristine FePt system can be related to the formation of the nonmagnetic shell on FePt NPs during hybrid formation. This is also confirmed from the upward increasing trend of FC magnetizations below 15 K for both hybrid systems.

Section B

5.5 Synthesis of magneto-fluorescent hybrid FePt@CdS nanosystem

The one pot direct synthesis of FePt@CdS core/shell hybrid nanosystem was based on a polyol process. In this synthesis procedure, GSH molecules were used as a sulfur source as well as a hydrophilic capping agent. In the initial step, FePt MNPs were synthesized (**Part C** of **Chapter 3**) in a conical flask under N_2 inert atmosphere and then cadmium source and GSH were added for the shell formation. For the development of FePt MNPs, 25 ml ethylene glycol, 1.0 mmol platinum (II) acetylacetonate, and 4 mmol sodium borohydride were added in a three-necked flask under N_2 atm. at room temperature [16]. After attaining the temperature 100 ºC, 2 mmol iron (III) acetylacetonate was added along with 200 µl of surfactant TGA. The solution in the same N_2 atm. was then heated up to 190 ºC at the rate of 1 °C per min. After that, the solution was cooled down to 80 °C temperature. At this point, the FePt nanoparticles were formed and were ready to act as a core for FePt@CdS hybrid nanosystem.
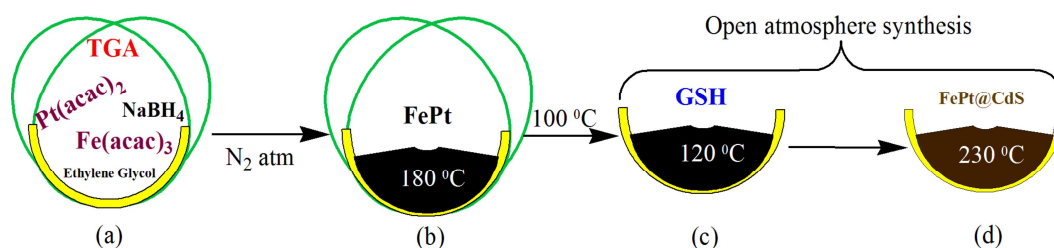

Figure 5.10 Schematic diagram represents synthesis of FePt@CdS hybrid nanosystem

The next step of the reaction was conducted in an open atmosphere. 2.5 mmol of cadmium chloride monohydrate and 0.5 mmol of GSH were dissolved in 5 ml of ethylene glycol separately where the molar ratio of Cd and GSH was maintained to 5:1. The inert atmosphere of the reaction vessel was removed when the reaction temperature came down to 100 °C. At first, the Cd precursor was added in the reaction vessel at this temperature 100 °C. After 15 minutes, 0.5 mmol glutathione was mixed in the reaction vessel elevated to a temperature of 120 °C, which acted as a capping agent as well as the

sulfur source. The reaction temperature was then further increased at the rate of 1 °C/min to 230 °C. After attaining 230 °C, the heating was stopped and the reaction vessel was allowed to cool down for the purification process.

The purification involved the separation of the precipitate from the reaction media via centrifugation and washing subsequently several times using hexane, isopropyl alcohol, and methanol to remove the residual surfactants. The purified mass obtained was brownish in color which was used in various characterizations.

5.6 Characterization

The synthesized QDs were characterized using several techniques for in-depth understanding of properties.

5.6.1 Results and discussion

Detailed structural and morphological study of the as-prepared hybrid nanosystem (FePt@CdS) was carried out using the analytical techniques like XRD, HRTEM, SAED, and EDX. The crystallographic structure of the FePt@CdS hybrid nanosystem was characterized by X-ray diffraction (XRD) using a Rigaku diffractometer with Cu K radiation (= 1.5406 Å). XRD pattern analysis reveals fcc FePt as well as hexagonal wurtzite phase CdS (JCPDS 89-2944) structure in the hybrid nanosystem.

Figure 5.11 indicates XRD pattern of the pristine and hybrid nanosystems. The diffractogram shows the presence of peaks at 2 ~ 24.8°, 26.5°, 28.1°, 36.6°, 43.6°, 47.8° and 51.8° corresponding to the (100), (002), (101), (102), (110), (103) and (112) orientation of hexagonal wurtzite phase CdS respectively [34].

XRD pattern analysis reveals that the structure is having lattice constant, a and c of values 0.4132 and 0.6715 nm respectively. It is seen that the lattice constant values are consistent with the standard values for CdS. However, the formation of CdO lattice in not observed in the XRD pattern of both the CdS and FePt@CdS nanosystems [26].
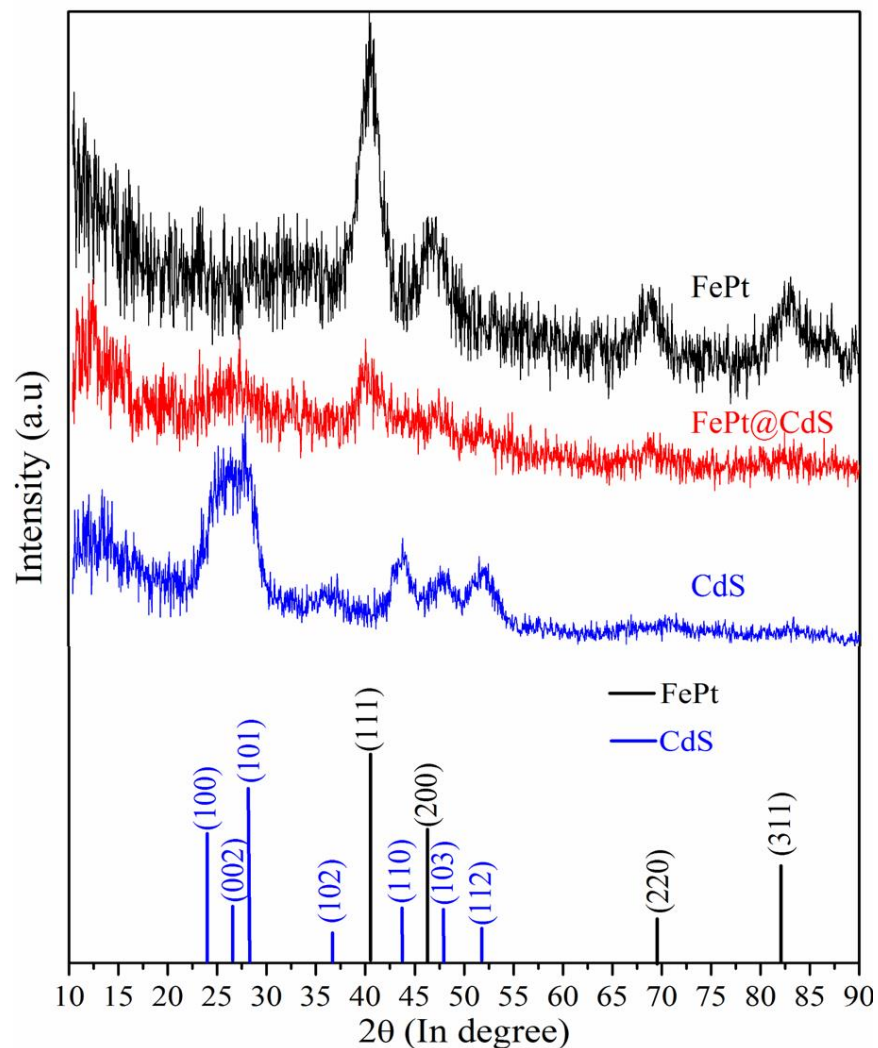
Figure 5.11 XRD patterns of FePt, and CdS and FePt@CdS nanosystem.

Figure 5.12 (a) shows the HRTEM micrograph of FePt@CdS hybrid nanosystem. From the micrograph, it is evident that in FePt@CdS system, the interplanar distance (d) value in the core is 0.22 nm which corresponds to the (111) plane of FePt. While the interplanar distance (d) observed in the shell is found to be 0.31 nm corroborating to the (101) plane of CdS crystal. In this system, FePt resides in the core while CdS is forming a shell. This result affirms the core-shell type of structure in FePt@CdS hybrid nanosystem. The SAED pattern analysis (inset of **figure 5.12 (a)**) reveals the presence of (111), (220) and (311) planes corresponding to fcc phase of FePt (JCPDS 29-0717) while only one plane (101) is revealed for hexagonal wurtzite phase CdS crystal.
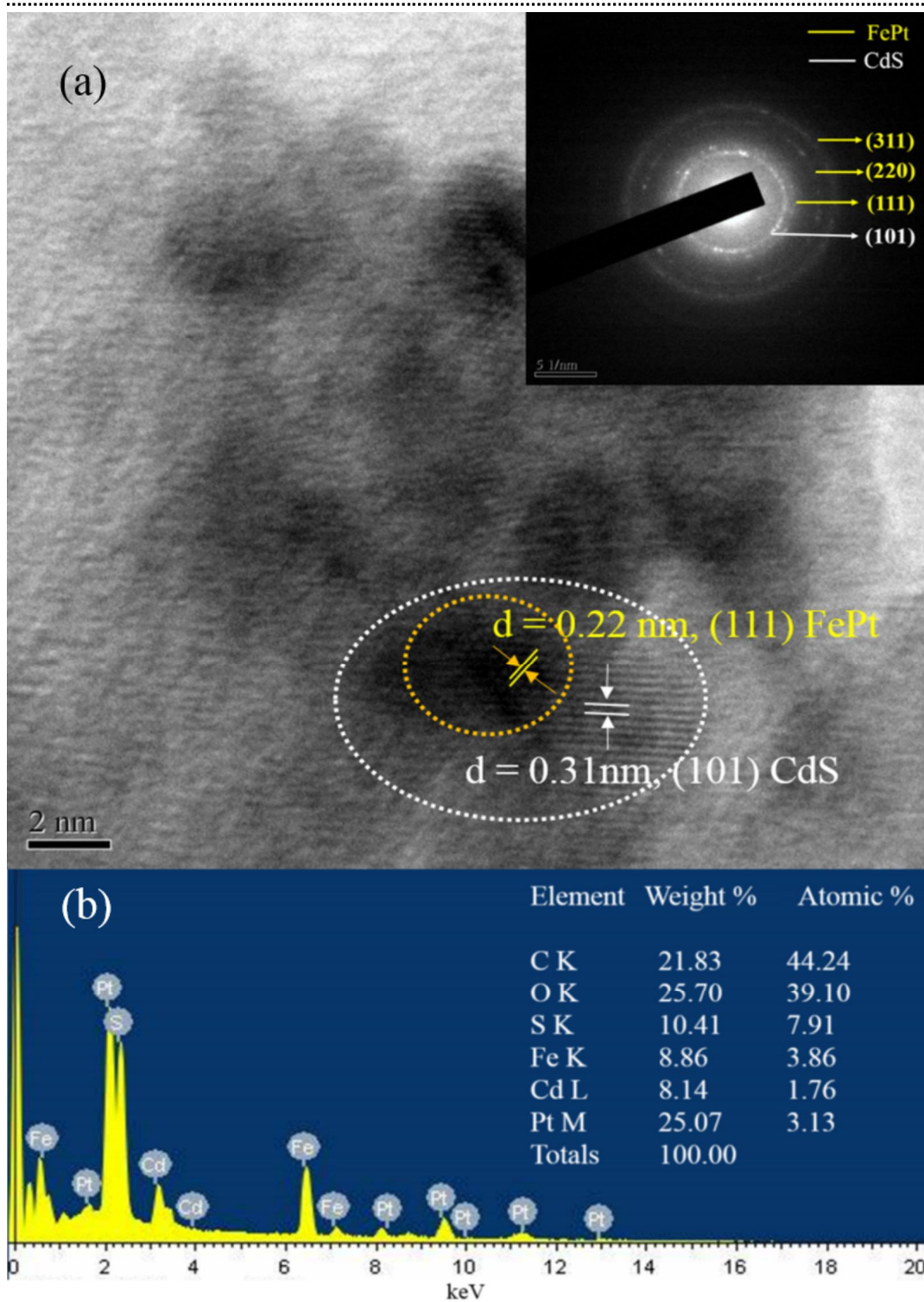
Figure 5.12 Microstructural and compositional characterization (a) HRTEM image and (b) EDX spectrum of FePt@CdS nanosystem. Inset in figure (a) depicts, SAED pattern of FePt@CdS hybrid nanosystem

The EDX spectrum of FePt@CdS expressed in **figure 5.12 (b)** indicates the main signature energy peak of the elements present in the sample - C (K line, 0.2 keV), O (K line, 0.5 keV), S (K line, 2.3 keV), Fe (L line, 0.7 keV; K line, 6.4 keV; K line, 7.1 keV), Pt (M line, 2.0 keV; L line, 9.4 keV;), and Cd (L line, 3.1 keV). The atomic weight % of the elements are also shown in the inset of **figure 5.12 (b)**. It is seen that the ratio of atomic percentage of S:Cd is 4.5:1 whereas Fe: Pt is ~ 1:1.

The surface composition and interaction of the surface coating molecule GSH with the hybrid (FePt@CdS) nanosystems were studied by FTIR spectroscopy, zeta potential and thermogravimetric analysis. The reaction was carried out in alkaline (pH 10) condition.
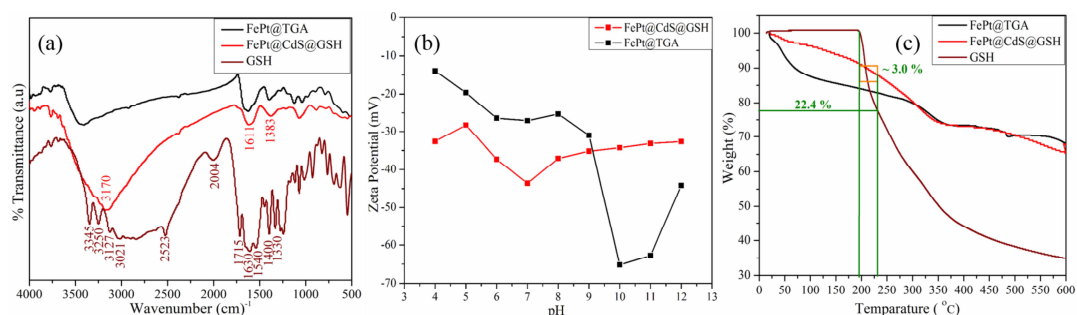

Figure 5.13 Surface characterizations of FePt@CdS hybrid nanosystem (a) comparative FTIR spectra of pure GSH, FePt@CdS, and FePt@TGA (b) zeta potential of FePt@CdS and FePt@TGA, (c) A comparative TGA study of pure GSH, FePt@CdS and FePt@TGA nanosystem

Figure 5.13 (a) represents the comparative FTIR spectra of pure GSH powder, TGA capped FePt and GSH capped FePt@CdS hybrid nanosystems. In case of pure GSH, a strong band at 2523 cm^{-1} is observed due to the -SH stretching vibrations. As seen in the earlier hybrid systems, the -SH band is absent in the FePt@CdS spectrum. It is due to the deprotonation of the thiol group and coordination of the thiol group to the surface of hybrid nanosystems. The combined bands of asymmetric NH$_3^+$ bending vibration and hindered NH$_3^+$ rotation at 2004 cm^{-1} seen in pure GSH disappeared in GSH capped FePt@CdS. This indicates the co-ordination of the amino group to the surface of hybrid nanosystems which is due to the deprotonation of an amino group. Also, the carboxylic C=O stretching vibration of the -COOH group at 1715 cm^{-1} in pure GSH molecule has come down to the lower frequencies possibly due to the deprotonation of -COOH group

in alkaline condition. In this hybrid system also, it is clearly evident that the characteristic C=O stretching (amide I) and N-H bending vibration (amide II) of amide bond emerged at 1630 and 1540 cm^{-1} in pure GSH molecule are merged into a single peak at 1611 cm^{-1} in FePt@CdS nanosystem. The disappearance of the -SH stretching vibrational peak, the almost disappearance of the N-H and the weakening of the amide bond clearly implies that the GSH molecules are coupling onto the surface of CdS through the -SH and -NHR groups [19-21].

Figure 5.13 (b) indicates the comparative zeta potential ( ) value of GSH capped FePt@CdS hybrid nanosystem and TGA capped FePt nanoparticle. The zeta potential within 4 to 12 pH gives an average negative potential value -35 mV which implies increased repulsion between nanoparticles and stability of hybrid nanosystems in aqueous solution. However, the   value is found to be around -45 mV at neutral pH. From the evident variation in the zeta potential of TGA capped FePt core system, the formation of CdS shell with GSH coating can be confirmed in the hybrid system.

The thermogravimetric analysis study of FePt coated with thioglycolic acid, pure GSH molecules and FePt@CdS hybrid nanosystem coated with glutathione is shown in **Figure 5.13 (c)**. The TGA curve shows two mass loss peaks at ~ 197 °C and 350 °C for both pure GSH and hybrid nanosystems arising due to the pyrolysis of the oxygenated functional groups and NHS moieties of GSH molecule respectively. It is seen that the FePt@CdS hybrid nanosystem starts to lose mass upon heating below 197 °C, which can be attributed to the loss of absorbed water molecules. At the synthesis temperature of 230 °C, pure GSH molecules lose ~ 22% of its mass. The hybrid nanosystems lose ~ 3 % mass within 197 to 230 °C, confirming the stability of GSH on hybrid nanosystems and absence of free GSH molecules after purification. A schematic model (**figure 5.14**) has been proposed which demonstrates the formation of the FePt@CdS system with a GSH coating.
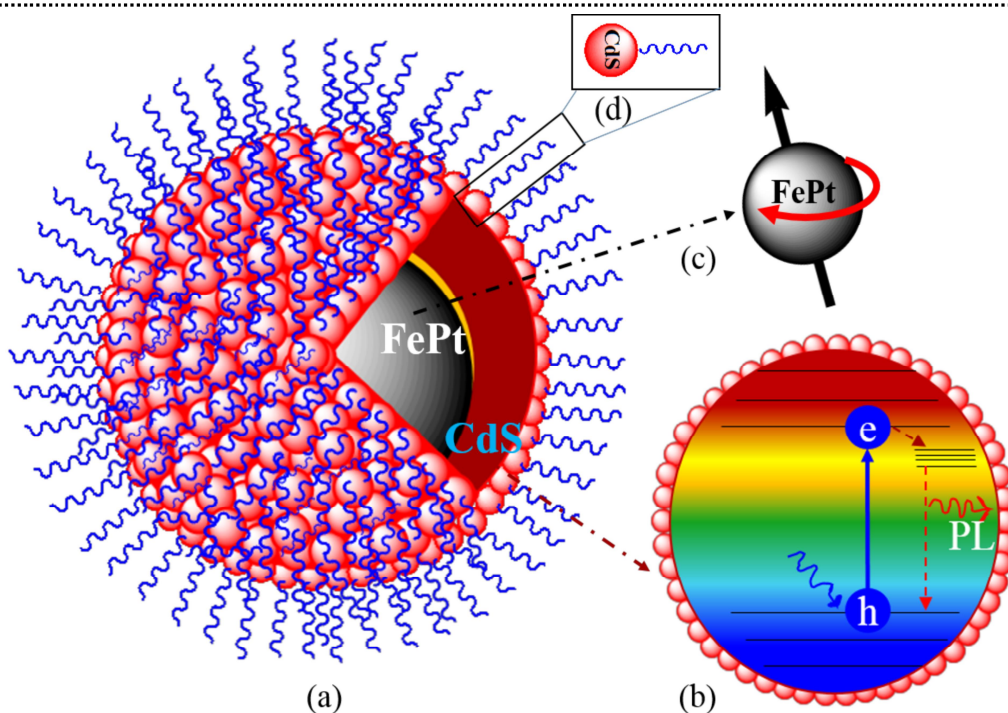
Figure 5.14 Schematic representation of model FePt@CdS nanosystem and shell CdS nanosystem. The model in (a) Core/shell of FePt/CdS (b) fluorescing shell (c) magnetic core (e) CdS layer due to GSH capping on the shell
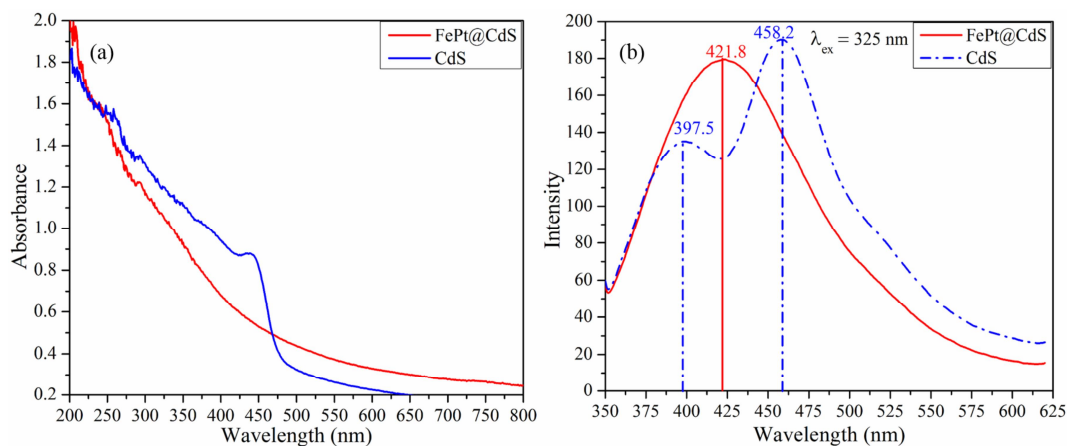

Figure 5.15 (a) UV-vis absorbance spectra of pristine CdS and hybrid FePt@CdS (b) PL spectra of CdS and FePt@CdS nanosystem in aqueous suspension. PL excitation wavelength was 325 nm

Figure 5.15 (a) and (b) indicates the UV absorption and corresponding photoluminescence (PL) spectra recorded at room temperature of pristine CdS QD and FePt@CdS hybrid nanosystems in aqueous dispersion. The capping agent efficiently

controls the size of particles and hence monodisperse particles of fine dimension are obtained. It is known that the band gap increases with the decrease in the size of the particle. UV-vis absorbance peaks are observed at 432 and 400 nm for CdS QD and FePt@CdS hybrid nanosystems whereas the bulk CdS reveal absorbance at ~ 516 nm [35]. This blue shift of the absorption edge indicates a decrease of the particle sizes of CdS QDs from bulk [35]. The blue shift also observed in FePt@CdS hybrid nanosystem as compared the pristine CdS QD. The UV-Vis absorbance curve of FePt@CdS w.r.t pristine CdS QD reveal indication of deposition over the magnetic core and formation of hybrid nanosystem.

In **figure 5.15 (b),** PL spectra of pristine (CdS QDs) observed are different from hybrid (FePt@CdS) nanosystem. Fluorescence spectra of the CdS QDs and FePt@CdS were measured with several excitation wavelengths from 225 to 350 nm. The fluorescence intensity has a little variation with excitation wavelength while the fluorescence peak center and band shape remain unchanged in both cases. This reveals that the emission spectra are almost independent of the excitation wavelength used. The maximum PL intensity has been obtained at $_{ex}$ = 325 nm in both cases. The fluorescence spectrum of CdS QDs shows a band edge emission at 397.5 nm and a broad trap state emission centered around 458 nm. For the FePt@CdS hybrid nanosystem, the PL spectrum has a single peak centered at 421.8 nm. This indicates that the trap state emission is less in hybrid (FePt@CdS) nanosystems than the pristine CdS QDs.

To understand the characteristic emissions, the PL spectrum of hybrid nanosystems is deconvoluted (**figure 5.16 (a)**). After Gaussian deconvolution, there are three peaks obtained around 398, 440 and 484.2 nm for FePt@CdS hybrid nanosystems. The pristine CdS QD system also exhibits three peaks at around 393, 456 and 485 nm. The first peak around 393 nm may be due to band edge emission, whereas the other two peaks around 440 nm and 485 nm are due the surface defect states. The CdS and FePt@CdS systems have not shown any significant shifting in the PL spectrum. This means that QDs with high band gap semiconductor like CdS are not likely to be easily modified during FePt@CdS hybrid formation [35]. The emission behavior of pristine (CdS) and hybrid (FePt@CdS) systems are also corroborating with the TRPL (time resolved photoluminescence) result in **figure 5.16 (b)**.
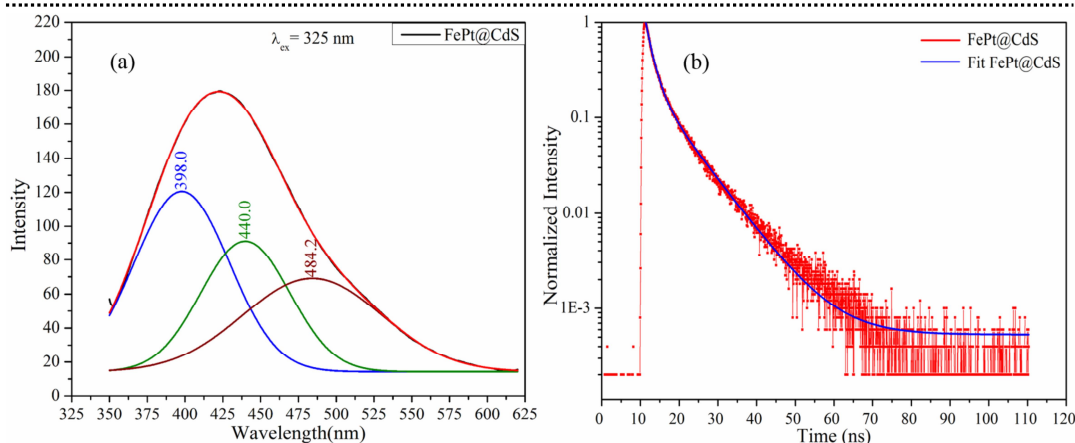
Figure 5.16 (a) Deconvoluted PL spectrum ($_{ex}$ = 325 nm), (b) TRPL spectrum of FePt@CdS hybrid nanosystem in aqueous suspension

TRPL spectrum was best fitted with the tri-exponential decay function as given below-

$$I = A_1 \exp\left(-\frac{t}{\tau_1}\right) + A_2 \exp\left(-\frac{t}{\tau_2}\right) + A_3 \exp\left(-\frac{t}{\tau_3}\right)$$

Where, I is the PL intensity, A_1, A_2 and A_3 represent the amplitudes of three decay processes, t-decay time, τ_1, τ_2 and τ_3 represent the three decay lifetimes. Values of lifetime components and their amplitudes (%) for each system are shown in **table 5.4**. The fast lifetime component might be due to the direct band-edge excitonic recombination while other longer components can be observed due to the radiative recombination of electrons and holes at localized surface states. Interestingly the average lifetimes of charge carriers are found to be increased from pristine to hybrid systems. The average lifetime for each TRPL data is calculated using the following equation:-

$$\langle \tau \rangle = \frac{\sum_i A_i \tau_i^2}{\sum_i A_i \tau_i}$$

*YS (%) - percentage amplitude of the fast component

*YL (%) - percentage amplitude of the longer component.

These are calculated using the equation

$$Y_i = \frac{A_i}{\sum_i A_i} \times 100$$

The increase in the average lifetime signifies the radiative emission stability of the systems [27, 28]. Thus, it can be told that the luminescence property has been improved significantly from pristine to hybrid systems and it is fascinated by a relative increment in the stable surface mediated emission.

Table 5.4 Decay components obtained from TRPL results for both pristine and hybrid nanosystems

Systems	Decay components						
	τ_1 (ns)	YS (%)*	τ_2 (ns)	YL$_1$ (%)*	τ_3 (ns)	YL$_2$ (%)*	$\langle \tau \rangle$ (ns)
CdS	0.764	72.8	2.859	21.77	8.70	5.34	3.8
FePt@CdS	0.35	57	2.15	30.76	8.39	12	5.34

The improved luminescent property is supported by the calculated quantum yield (QY) values shown in **table 5.5**, whereas, fluorescence micrographs of pristine QDs and hybrid nanosystems are shown the in the **figure 4.18 (section B; chapter 4)** and **figure 6.6** in next chapter respectively.

Table 5.5 Comparative Quantum yield (QY) values of pristine and hybrid nanosystems.

S. No	Systems	Quantum Yield (%)
1	CdS	1.67
2	FePt@CdS	1.71

Figure 5.17 (a-c) shows the temperature dependent M-H curves for FePt@CdS hybrid nanosystem and pristine FePt MNPs. The coercivity of FePt@CdS hybrid nanosystem increases linearly with decreasing temperature and attains the maximum at 20 K. The increased coercivity is the result of increased anisotropy energy barriers with decreasing temperature. But, at room temperature (RT), the coercivity of pristine and FePt@CdS hybrid nanosystem are not significantly different, and it is around 20 Oe. At RT, saturation magnetization for pristine (FePt) and hybrid nanosystem (FePt@CdS) has not

been attained up to 9 T. The increasing saturation magnetization (Ms) with decreasing temperature for hybrid system can be corroborated with decrease in thermal energy. The reduction in M_s of FePt@CdS can be attributed to the surface spin disorder due to capping with a nonmagnetic shell (CdS) [31]. **Figure 5.17 (d)** elucidates the M-T measurements (ZFC and FC) of pristine and hybrid nanosystem with probe field 100 Oe. The difference between T_{max} (maximum temperature in the ZFC curve) and T_{irr} (irreversibility temperature) reflects the nanoparticle size distribution in FePt@CdS hybrid nanosystem as compared to the pristine one. Moreover, the observed Curie behavior of ZFC and FC curves above the blocking temperature implies the negligible inter-particle interaction in both the samples.
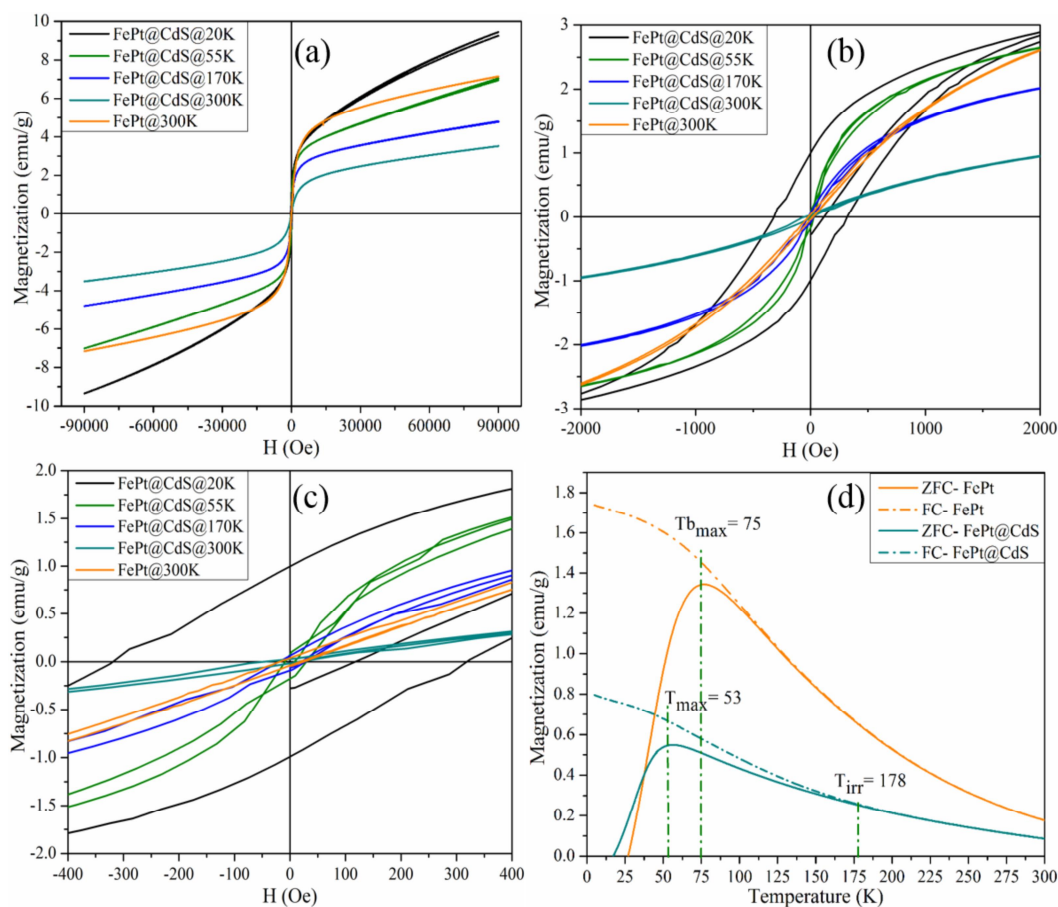

Figure 5.17 Magnetic characteristics of FePt@CdS hybrid nanosystem with pristine FePt MNPs (a-c) field dependent (M-H) magnetization curve with (a) 9 T (b) 2 T (c) magnified view of the region close to the zero field (d) temperature dependent (M-T) magnetization curve

The T_b of FePt@CdS (~53 K) is lower than that of FePt MNPs (~75 K). The decrease in the value of T_b can be explained by lowering of the magnetic anisotropy energy. This decrement can be correlated to the lowering of dipole-dipole interaction in the hybrid system due to a nonmagnetic shell. This result also affirms the core-shell type of structure in FePt@CdS hybrid nanosystem. Due to low coercivity and T_b value, both FePt and FePt@CdS hybrid nanosystem exhibits ferromagnetic behavior at 5 K and superparamagnetic behavior at RT.

5.7 Conclusion

The integration of fluorescence imaging (FI) with MR imaging (MRI) is a significant step towards the development of innovative noninvasive imaging techniques. TGA capped FePt nanoparticles were used for the development of the magneto-fluorescent hybrid nanosystems with CdTe, CdSe, and CdS quantum dots as the fluorescent counterparts. These complex hybrid structures were developed through a facile one-pot polyol method. Hybrid nanosystems were stabilized with GHS capping agent, which is known for major physiological functions such as detoxification, redox-buffering, and antioxidant activity. The zeta potential results showed negative charge on all three hybrid systems and hydrophilic stability. Interestingly, calculated quantum yields for all three hybrid nanosystems were obtained to be higher than that of the pristine quantum dot systems. Moreover, the magnetization values for the hybrid systems were compromised significantly after hybrid formation. The reduction in Ms for hybrid nanosystems can be attributed to the surface spin disorder due to capping with a nonmagnetic shell (CdTe, CdSe, and CdS). It is also observed that high band gap semiconductor nanocrystals are not likely to be modified during the hybrid formation. Extremely low values of coercivity and remanence along with the obtained blocking temperature well below the room temperature signify the superparamagnetic characteristic of the developed hybrid nanosystems. These hybrid nanosystems provide a single entity with a multifunctional attribute which can be used for simultaneous optical and magnetic resonance imaging.

References:

[1] Gu, H. *et al.* Biofunctional magnetic nanoparticles for protein separation and pathogen detection. *Chem. Commun. (Camb).* (9), 941--949, 2006. doi:10.1039/b514130c.

[2] Bao, J. *et al.* Bifunctional Au-Fe3O4 nanoparticles for protein separation. *ACS Nano* **1** (4), 293--298, 2007.

[3] Ito, A. *et al.* Medical application of functionalized magnetic nanoparticles. *J. Biosci. Bioeng.* **100** (1), 1--11, 2005.

[4] Pankhurst, Q. A. *et al.* Applications of magnetic nanoparticles in biomedicine. *Journal of Physics D: Applied Physics* **36** (13), R167--R181, 2003.

[5] Hafeli, U. O. *et al.* Cell uptake and *in vitro* toxicity of magnetic nanoparticles suitable for drug delivery. in *Molecular Pharmaceutics* **6** (5), 1417--1428, 2009.

[6] Bhirde, A. *et al.* Nanoparticles for cell labeling. *Nanoscale* **3** (1), 142--153, 2011.

[7] Yoo, D. *et al.* Theranostic magnetic nanoparticles. *Acc. Chem. Res.* **44** (10), 863--874, 2011.

[8] Aptekar, J. W. *et al.* Silicon nanoparticles as hyperpolarized magnetic resonance imaging agents. *ACS Nano* **3** (12), 4003--4008, 2009.

[9] Yang, L. *et al.* Receptor-targeted nanoparticles for *in vivo* imaging of breast cancer. *Clin. Cancer Res.* **15** (14), 4722--4732, 2009.

[10] Bals, S. *et al.* Three-dimensional atomic imaging of colloidal core-shell nanocrystals. *Nano Lett.* **11** (8), 3420--3424, 2011.

[11] Torigian, D. A. *et al.* PET/MR imaging: technical aspects and potential clinical applications. *Radiology* **267** (1), 26--44, 2013.

[12] Pichler, B. J. *et al.* PET/MRI hybrid imaging: Devices and initial results. *Eur. Radiol.* **18** (6),1077--1086, 2008.

[13] Judenhofer, M. S. *et al.* Simultaneous PET-MRI: a new approach for functional and morphological imaging. *Nat. Med.* **14** (4), 459--465, 2008.

[14] Talapin, D. V. *et al.* CdSe/CdS/ZnS and CdSe/ZnSe/ZnS core-shell-shell nanocrystals. *J. Phys. Chem. B* **108** (49), 18826--18831, 2004.

[15] De Donatis, G. M. *et al*. Cysteinyl-glycine in the control of glutathione homeostasis in bovine lenses. *Mol. Vis.* **16** , 1025--1033, 2010.

[16] Jha, D. K. *et al.* Direct synthesis of water dispersible superparamagnetic TGA capped FePt nanoparticles: One pot, one shot. *Mater. Chem. Phys.* **156**, 247--253, 2015.

[17] Dorfs, D. *et al.* Type-I and type-II nanoscale heterostructures based on CdTe nanocrystals: A comparative study. *Small* **4** (8), 1148--1152, 2008.

[18] Pérez-Donoso, J. M. *et al.* Biomimetic, mild chemical synthesis of Cdte-GSH quantum dots with improved biocompatibility. *PLoS One* **7** (1), e30741--e30749, 2012.

[19] Reis, E. F. dos *et al.* Synthesis and characterization of poly (vinyl alcohol) hydrogels and hybrids for rMPB70 protein adsorption. *Mater. Res.* **9** (2), 185--191, 2006.

[20] Wang, Q. *et al.* Direct synthesis of high-quality water-soluble CdTe:Zn^{2+} quantum dots. *Inorg. Chem.* **51** (17), 9208--9213, 2012.

[21] Zhang, J. *et al.* Aqueous synthesis of ZnSe nanocrystals by using glutathione as ligand: The pH-mediated coordination of Zn^{2+} with glutathione. *J. Phys. Chem. C* **114** (25), 11087--11091, 2010.

[22] Ferretti, L. *et al.* Glutathione and N-acetylcysteinylglycine: Protonation and Zn^{2+} complexation. *J. Inorg. Biochem.* **101** (10), 1442--1456, 2007.

[23] Leverrier, P. *et al.* Metal binding to ligands: Cadmium complexes with glutathione revisited. *Anal. Biochem.* **371** (2), 215--228, 2007.

[24] Pu, F. & Ren, J. Lighting up silica nanotubes transcribed from the submicron structure of a metalópeptide hybrid. *Nanotechnology* **24** (2), 375603-375612, 2013.

[25] Murray, C. B. *et al.* Synthesis and characterization of nearly monodisperse CdE (E= S, Se, Te) semiconductor nanocrystallites. *J. Am. Chem. Soc.* **115** (4), 8706--8715, 1993.

[26] Trinh, T. T. *et al.* One-pot synthesis and characterization of well defined core-shell structure of FePt@CdSe nanoparticles. *RSC Adv.* **1**, 100--108, 2011.

[27] Schlegel, G. *et al.* Fluorescence Decay Time of Single Semiconductor Nanocrystals. *Phys. Rev. Lett.* **88** (13), 137401--137404, 2002.

[28] Nirmal, M. *et al.* Observation of the Dark Exciton in CdSe Quantum Dots. *Phys. Rev. Lett.* **75** (20),3728--3731, 1995.

[29]   Taniguchi, S. *et al.* The one-pot synthesis of core/shell/shell CdTe/CdSe/ZnSe quantum dots in aqueous media for *in vivo* deep tissue imaging. *J. Mater. Chem.* **21** (9), 2877--2882, 2011.

[30]   Sytnyk, M. *et al.* Tuning the magnetic properties of metal oxide nanocrystal heterostructures by cation exchange. *Nano Lett.* **13** (2), 586--593, 2013.

[31]   Gao, J. *et al.* Fluorescent magnetic nanocrystals by sequential addition of reagents in a one-pot reaction: A simple preparation for multifunctional nanostructures. *J. Am. Chem. Soc.* **129** (39), 11928--11935, 2007.

[32]   Siah, W. R. *et al.* Quantum Dot Growth on Magnetic Nickel Nanoparticles. *Cryst. Growth Des.* **13** (6), 2486--2492, 2013.

[33]   Kale, A. *et al.* Magnetite/CdTe magnetic-fluorescent composite nanosystem for magnetic separation and bio-imaging. *Nanotechnology* **22** (22), 225101--225111, 2011.

[34]   Kobayashi, Y. *et al.* Effect of Surface Defects on Auger Recombination in Colloidal CdS Quantum Dots. *J. Phys. Chem. Lett.* **2** (9), 1051--1055, 2011.

[35]   Wu, Y. *et al.* Charge-sensitive Surface Optical Phonon in CdS Quantum Dots Studied by Resonant Raman Spectroscopy. *J. Phys. Chem. C* **118** (51), 30269--30273, 2014.